universe

MDPI

Article

Low-Latitude Ionospheric and Geomagnetic Disturbances Caused by the X7.13 Solar Flare of 25 February 2014

Zane Nikia C. Domingo [1], Ernest P. Macalalad [1,*] and Akimasa Yoshikawa [2]

[1] Department of Physics, Mapua University, Intramuros, Manila 1002, Philippines; zncdomingo@mymail.mapua.edu.ph
[2] International Center for Space Weather Science and Education, Kyushu University, Fukuoka 812-8581, Japan; yoshikawa.akimasa.254@m.kyushu-u.ac.jp
* Correspondence: epmacalalad@mapua.edu.ph

Abstract: On 25 February 2014 at around 00:39 UT, a major solar flare (code: SOL2014-02-25T00:39) erupted at sunspot region AR11990. Using the updated science quality data of GOES-15, it has been classified as an X7.13 solar flare. This gave rise to the electron density changes that affected the strengths of ionospheric electric currents. In this work, the difference in total electron content (TEC), between the TEC during a flare day and a quiet, fitted TEC, ΔTEC, and rate of change of TEC, $dTEC/dt$, are determined to observe electron density changes due to the solar flare over a low-latitude region. These stations are at Quezon City (PIMO) and Taguig City (PTAG). Also, responses in the geomagnetic field component, ΔH, are calculated along with the variations in the equatorial electrojet (EEJ) strength. These are observed at equatorial, Davao (DAV) and Cagayan de Oro (CDO), and off-equatorial, Muntinlupa (MUT) and Legazpi (LGZ), stations. The resulting ΔTEC values were 1.17–1.97 TECU while $dTEC/dt$ maxima were 0.29–0.48 TECU/min. The $dTEC/dt$ maxima were found to concur with the time the solar EUV reached peak intensity at 00:45 UT, 4 min before the flare (i.e., X-ray) peaked. Furthermore, the ΔH variations exhibited larger enhancements at the equatorial stations. These are mostly attributed to the EEJ contributing to the geomagnetic field variations. The amplification experienced by the EEJ due to the increased ionospheric conductivity is then reflected in the geomagnetic responses. For the CDO-LGZ stations, the EEJ strength reached ~37 nT, while for the DAV-MUT, this was ~60 nT.

Keywords: solar flare; low latitude; ionosphere; space weather; total electron content; geomagnetic field

Academic Editor: Dmitrii Kolotkov

Received: 25 November 2024
Revised: 20 January 2025
Accepted: 22 January 2025
Published: 17 February 2025

Citation: Domingo, Z.N.C.; Macalalad, E.P.; Yoshikawa, A. Low-Latitude Ionospheric and Geomagnetic Disturbances Caused by the X7.13 Solar Flare of 25 February 2014. *Universe* **2025**, *11*, 70. https://doi.org/10.3390/universe11020070

1. Introduction

Incoming solar radiation is absorbed by the Earth's upper atmosphere, by which heating and ionization are initiated [1]. The region where this ionization is mainly maintained is known as the ionosphere forming the D, E, and F regions [2]. The numerous impacts of solar radiation on Earth demonstrate that there are many ways to observe solar–planetary interactions, especially during high solar activities. When the Sun is immensely active, there are more phenomena that entail enhanced solar radiation. The release of such radiation is primarily involved during the occurrence of solar flares which are explosive processes in the Sun's atmosphere [3,4]. These extreme eruptions are classified based on the peak X-ray flux (W/m^2) in the 0.1–0.8 nm range.

Aside from geomagnetic storms, solar flares also cause disturbances in the ionosphere on the sunlit side. These transient increases in electromagnetic solar radiation can be observed in different frequencies and wavelengths [5]. In studying the ionospheric and

magnetospheric effects of such eruptions, the X-ray and EUV bands are mostly used. In measuring the ionospheric responses to solar flares, the Total Electron Content (TEC) in TECU units (10^{16} electrons/m^2) is a key parameter used to determine the number of electrons along the path of the signal from the satellite through the ionosphere and eventually to the receiver.

It is crucial to know that the ionosphere is an open system because it is also coupled with the magnetosphere. Electric currents flow globally throughout the ionosphere and magnetosphere [6]. Such electrodynamic coupling is mostly understood when electric currents flow across the magnetic field lines in the ionosphere, extending to the outer magnetosphere [7].

Other ways of monitoring the TEC over the Philippines have also been explored in previous years. Maglambayan et al. [8] constructed regional TEC maps via kriging interpolation. They were able to recreate these maps for different ionospheric conditions including scintillations, quiet days, and geomagnetic storms. On the other hand, a study made by Mendoza et al. [9] focused on the TEC enhancements during a series of solar flares in 2017 as well as the presence of geomagnetic storms. Their observations made use of GNSS stations over the Philippines (PIMO, PPPC, PGEN) and Taiwan region (TQTF, CKSV). These overall show that TEC enhancements are exhibited even for different space weather conditions. Some of these also may be accompanied by other solar phenomena. In the present work, we firstly show that solar flares, as just the primary driver, are efficient in generating changes in the ionospheric electron density.

Moreover, Earth's own magnetic field is also responsive to ionospheric changes due to increased solar radiation. Short-lived disturbances in the geomagnetic field components, known as solar flare effects (Sfe), sometimes accompany solar flares. The Sfe variations are also interpreted as temporary enhancements in the geomagnetic diurnal variations caused by the anomalies in the electric conductivity increase [10].

It is established that ionospheric currents account for a fraction of the observed geomagnetic field. Among these is the ionospheric Solar-quiet (Sq) current that is responsible for the regular diurnal variations in the geomagnetic field [11]. The associated Sq variations have been crucial in studying ionospheric electrodynamics [12] and its electrodynamic coupling to the magnetosphere and atmosphere [13]. During low geomagnetic activities, the Sq current system, extending from 90 to 150 km in the E-region [14], is mostly dominant. When there are no disturbances such as geomagnetic storms that dwarf the Sq signals, the Sfes stand out more. The Sq morphology on the dayside view appears as two loops or vortices with two foci in each hemisphere [15]. The foci are near the middle latitudes, and in the magnetic equator, the Sq feeds into the Equatorial Electrojet (EEJ). This EEJ is a narrow latitudinal band of eastward electric current [16], which likewise flows in the E-region maximizing at 105 km [17]. Within the electrojet, there is a large current density that is primarily caused by the locally enhanced ionospheric Cowling conductivity [16]. This brings about the strong zonal currents of the EEJ [11,18]. Additionally, these currents cause amplification of the Sq variations associated with the magnetic responses for ground-based observatories near the equator [19].

During normal electrojet conditions, enhancements in the H component are reported to be simultaneous with solar flare events. Gopika et al. [20] investigated the ΔH variations during an M1.5 flare (20 February 2022) and X1.9 (24 September 2011) flare. A positive Sfe was observed during the flare peak during both events; however, a reversed Sfe (reduction in the ΔH) was noticed soon after the flare peak of the M1.5 flare. Here, they have used model calculations to show the conductivity ratio in the D- and E-regions, resulting in modifications in the current systems that generate different signatures on the ΔH. During an intense X-class flare, the TEC enhancements were also investigated by Sripathi et al. [21].

Included also were the changes in the ΔH component at low-latitude and equatorial stations attributable to the electrojet strengths.

In this study, the ionospheric and geomagnetic responses to increased solar radiation during an X7.13 solar flare (code: SOL2014-02-25T00:39) on 25 February 2014 are investigated. TEC calculations are performed and the increases observed during the flare are quantified. The geomagnetic variations, limited to the H component, are also graphed. Equatorial and off-equatorial stations over the Philippines are used for the geomagnetic measurements. Thus, the existence of the EEJ and its contribution are also given more focus.

2. Data and Methods

The solar X-ray and EUV data were acquired from the National Oceanic and Atmospheric Administration (NOAA) Geostationary Operational Environmental Satellites (GOES) archives. The data are from the science quality GOES-15 XRS Level 2 product [22]. The X7.13 solar flare that erupted over the sunspot region AR11990 on 25 February 2014 of solar cycle 24 is selected for this study. This was also the strongest solar flare in 2014. The short (0.5–4 Å, XRSA) and long (1–8 Å, XRSB) wavelengths for the X-ray and 121.6 nm for the EUV are considered. Additional EUV photon flux measurements from the Solar EUV Monitor (SEM) instrument of the Solar and Heliospheric Observatory (SOHO) were also used for the 26–34 nm and 0.1–50 nm bands.

The X7.13 flare corresponds to an R3 radio blackout based on NOAA Scales. It started at 00:39 UT and reached its peak at 00:49 UT. It returned to an M5 level (10^{-4} Wm^2) at 01:31 UT, and this corresponds to an R2 radio blackout. In this instance, its severity is considered moderate as reflected in radio blackout impacts [23]. Cutting off the observation time at M5 is undertaken because anything lower than M5 only experiences minor or weak radio blackouts (R1). These effects are seen in weak degradation of high-frequency radio communication on the sunlit hemisphere, loss of contact in radio, and degradation of low-frequency navigation signals for temporary intervals [24].

Geomagnetic conditions during this event are determined using the Kp, Hp (Hp30 and Hp60), and Dst indices [25]. Both Kp and Hp values were accessed from the GFZ German Research Centre for Geoscience [25,26]. The Dst values, on the other hand, were accessed from the NASA/Goddard Space Flight Center OMNIWeb Archives.

Figure 1 shows the superimposed measurements for the three geomagnetic indices. The observation time is from 21:00 UT on the previous day (24 February 2014) until 06:00 UT on the flare day. The primary indicator in ensuring low geomagnetic disturbances is the max Kp to be $\leq$3. Around the time of the flare maximum, the maximum Kp value reached 0.667 and the Dst minimum reached over $-$13 nT. The Hp measurements are also relatively consistent with the Kp, further confirming the quiet geomagnetic conditions.

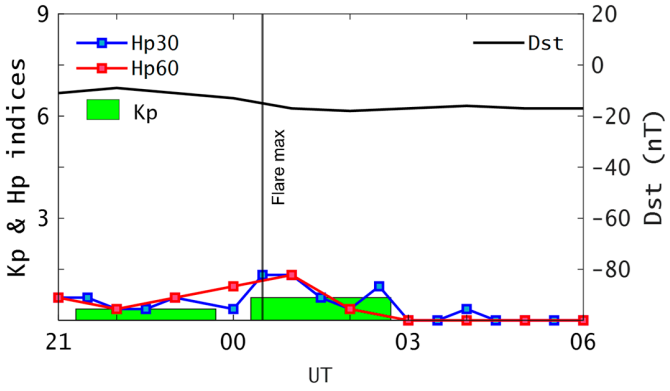

Figure 1. Geomagnetic conditions during the X7.13 flare (25 February 2014) using the Kp, Hp, and Dst indices.

Moreover, the data acquisition for the TEC is obtained using the dual-frequency Global Navigation Satellite System (GNSS) data [27]. The Relative Slant TEC (*STEC*) makes use of frequencies, f_1 (1565.42 MHz) and f_2 (1227.60 MHz), and carrier-phase measurements (L_1 and L_2), the calculation for which is given by Equation (1) [28].

$$STEC = \frac{1}{40.3}\frac{f_1^2 f_2^2}{f_1^2 - f_2^2}(L_1 - L_2) \quad (1)$$

Equation (2) shows how the Relative *STEC* is converted to the Relative Vertical TEC (*VTEC*) by using a mapping function $S(E)$. The mapping function is given by Equation (3), where R_E is Earth's radius (6371 km), H is the assumed ionospheric pierce point shell height (450 km), and E is the satellite elevation angle (in degrees). The shell height of 450 km is within the range that is considered when the data is fitted [29].

$$VTEC = STEC \times S(E) \quad (2)$$

$$S(E) = \left(1 - \left(\frac{R_E \times \cos(E)}{R_E + H}\right)^2\right)^{1/2} \quad (3)$$

To emphasize the change observed during solar flares in the TEC calculations during flare events, the TEC during a quiet day is superimposed with that of the flare day. The time derivatives ($dTEC/dt$) of those TEC calculations are also calculated to further magnify the difference between the ionospheric behaviors during a flare and a quiet day. In addition to quantifying the TEC change, a cubic spline interpolation is applied to determine a background TEC that is to be subtracted from the actual TEC data to get the ΔTEC. The cubic spline function in the TEC calculations was also used in studies made by Chen et al., Ansari et al., and Maletckii et al. [30–32]. The assigned limit for the interpolation for the X7.13 flare is from the time the $dTEC/dt$ first rises until the arrival at the M5 level.

As for the magnetometer data, these were acquired from SuperMAG [33,34]. In analyzing the geomagnetic variations for the H component, the baseline data are determined by taking the average of the values at local midnight (16:00 UT) extended to two hours before and after (14:00 UT, 15:00 UT, 17:00 UT, 18:00 UT). This baseline is subtracted from the data to determine the magnetic field, thus the ΔH. This is to isolate the EEJ from any other existing influences. The EEJ strength (nT) is then calculated by finding the difference between the ΔH at the equatorial and off-equatorial stations [35], as given by Equation (4).

$$EEJ\ (\text{nT}) = \Delta H_{(\text{Equator})} - \Delta H_{(\text{Off-equator})} \quad (4)$$

Figure 2 shows the map that encompasses all the stations over the Philippines used in the study. Magnetometer stations (SuperMAG) include Davao (station code: A08), Muntinlupa (MUT), Cagayan de Oro (CDO), and Legazpi (LGZ). The equatorial stations are A08 (geographic coordinates: 7° N, 124° E, dip lat: −0.107°) and CDO (8.4° N, 124.6° E, dip lat: 3.163°) [33,34]. By contrast, the off-equatorial stations are MUT (14.37° N, 121.02° E, dip lat: 16.936°) and LGZ (13.1° N, 123.7° E, dip lat: 13.733°). The dip latitudes are based on the 13th model of the International Geomagnetic Reference Field.

Moreover, the GNSS stations include PIMO, at Quezon City, and PTAG, at Taguig City. PIMO (14.63° N, 121.07° E, dip lat: 17.484°) and PTAG (14.53° N, 121.04° E, dip lat: 17.275°) stations are at the low-latitude region.

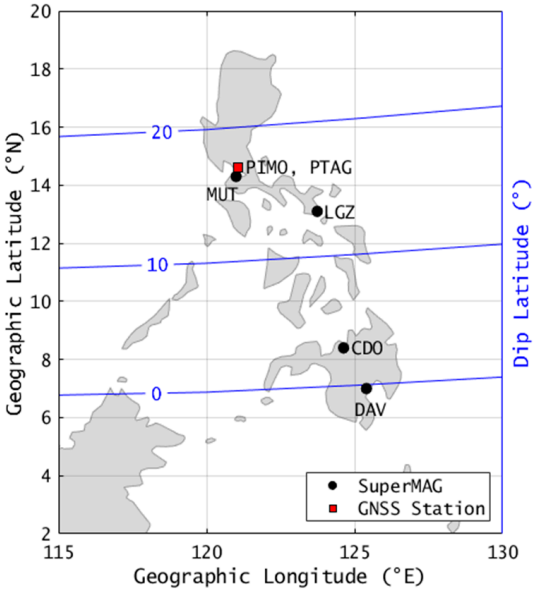

Figure 2. A map of stations used include the GNSS stations (red squares) and SuperMAG stations (black circles). The geographic coordinates are specified on the left axis and x-axis while the dip latitude (blue lines) is on the right axis.

3. Results and Discussions

3.1. Solar X-Ray and EUV

The X7.13 flare was originally classified as an X4.9 using GOES-15 operational data. It was re-classified as an X7.13 with the science quality data after reprocessing methods had been made. The solar X-ray and EUV fluxes in W/m^2 are shown in Figure 3. The differently colored vertical lines represent the time at which the flare began (00:39 UT), reached its maximum (00:49 UT), and returned to an M5 level (01:31 UT). The EUV flux at 121.6 nm peaked at around 00:45 UT, 4 min before the flare peaked using the GOES data. It increased to 93.7×10^{-4} W/m^2 from its background value of about 84×10^{-4} W/m^2. On the other hand, the EUV count measurement reached peak enhancements at 00:52 UT for the narrow (26–34 nm) and broad (0.1–50 nm) bands, 3 min after the peak of the flare. For the narrow band, this increased to 2.23×10^{10} photons-$cm^{-2}s^{-1}$ from 1.88×10^{10} photons-$cm^{-2}s^{-1}$. Whereas for the broad band, this increased to 6.78×10^{10} photons-$cm^{-2}s^{-1}$ from 3.81×10^{10} photons-$cm^{-2}s^{-1}$. Counts in both bands started rising at the time the EUV irradiance reached its peak. The broader band is also shown to have prolonged enhancements.

It is also observed that the peak that corresponds to the 121.6 nm is sharper than the peaks of the two bands, 26–34 nm and 0.1–50 nm. This sharpness is found to be more typical for longer than for shorter wavelengths [36]. This does not necessarily follow the bandwidth. Moreover, according to Pandey et al. [37], the solar flare event in the present study experienced impulsive and gradual EUV peaks at 00:46 UT and 00:51 UT, respectively. These all happened differently with respect to the time at which the flare peaked.

Along with the increases in the solar X-ray, the evident changes in the EUV, are the sources of ionization in the ionosphere, which grow more significant during the X7.13 flare. It is known that the X-ray mostly contributes to the ionization at low altitudes where the D-region is, while the EUV mostly dominates the E- and F-regions. This will be further discussed in the following sections.

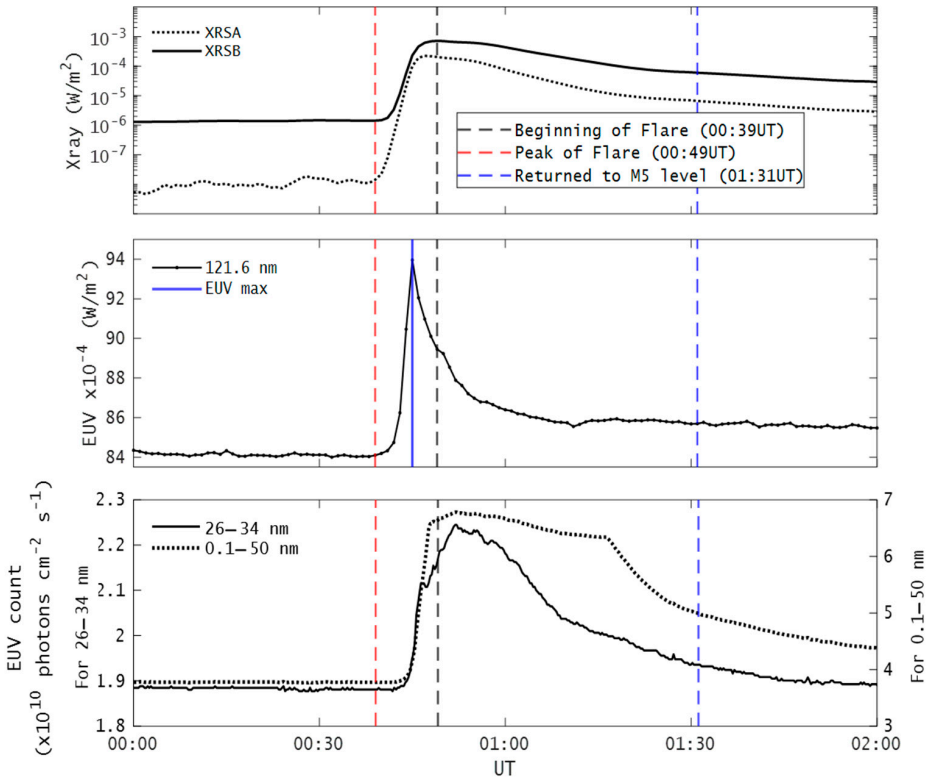

Figure 3. Solar radiation during X7.13 (25 February 2014) for X-ray in long (1–8 , XRSB) and short (0.4–5 , XRSA) wavelengths, EUV flux in 121.6 nm (GOES) in addition to the 26–34 nm and 0.1–50 nm bands.

3.2. Total Electron Content

The calculated Relative TEC in TECU at PTAG is shown in Figure 4. In particular, the Relative TEC measurements during the flare day (25 February 2014) and quiet day (26 February 2014) are shown in Figure 4a. The response signature exists for the flare day. They are observed approximately 5 min before the flare maximum, whereas no noticeable changes exist for the quiet day, as expected. The changes for the flare day are further quantified using the ΔTEC, as shown in Figure 4b right axis.

At PTAG, the maximum ΔTEC values are determined to be 1.75, 1.52, and 1.97 TECU for PRNs 2, 5, and 15, respectively. These measurements were also made for PIMO, as shown in Figure 5. Similarly, the signature of changes that arises at around 00:44 UT exists only during the flare day, which is contrasted with the quiet day. The onset of this rise is around 5 min before the flare maximum. From the right axis of Figure 5b, the maximums of the ΔTEC values at PIMO are determined to be 1.17, 1.31, and 1.56 TECU for PRNs 2, 5, and 15, respectively. At both stations, it can be consistently ascertained that the instant the TEC rises toward maximum before the flare maximizes. The ΔTEC reveals the highest increase shortly after the flare maximum.

Saharan et al. (2023) [38] showed that a first-order polynomial via baseline and mean methods yielded a correlation between the ΔDVTEC and ΔEUV for X-class flares. They have also shown that the ΔEUV flux has a stronger correlation than the ΔXRay with the ΔDVTEC. In both cases, the values decreased with the flare class.

In the present analysis, the $dTEC/dt$ measurements are determined to further see the responses in the ionosphere with respect to the time at which the EUV maximizes. The $dTEC/dt$ for each PRN is shown at PTAG in Figure 6a and PIMO in Figure 6b. There is also a vertical line that indicates the time at which the EUV reached apex, which is at 00:45 UT, four minutes only before the flare peak.

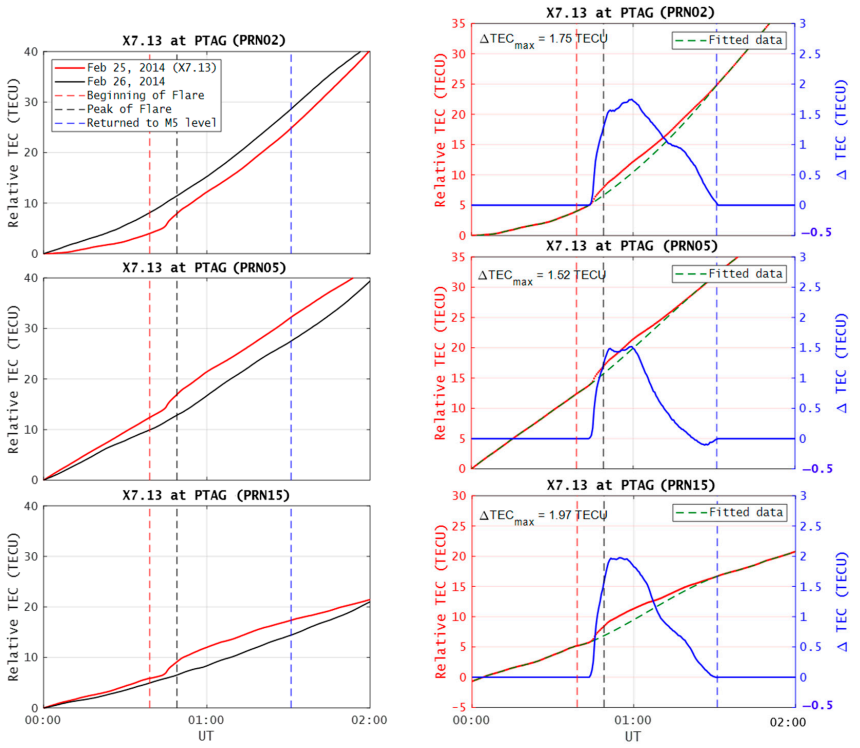

(**a**) (**b**)

Figure 4. (**a**) Superimposed Relative TEC for 25 February (flare day) and 26 February 2014 with the time markers at PTAG; (**b**) (Left axis) Relative TEC for the flare day superimposed with the fitted data and (Right axis) the ΔTEC for the flare day curve. Observation time is from 00:00 UT to 00:02 UT.

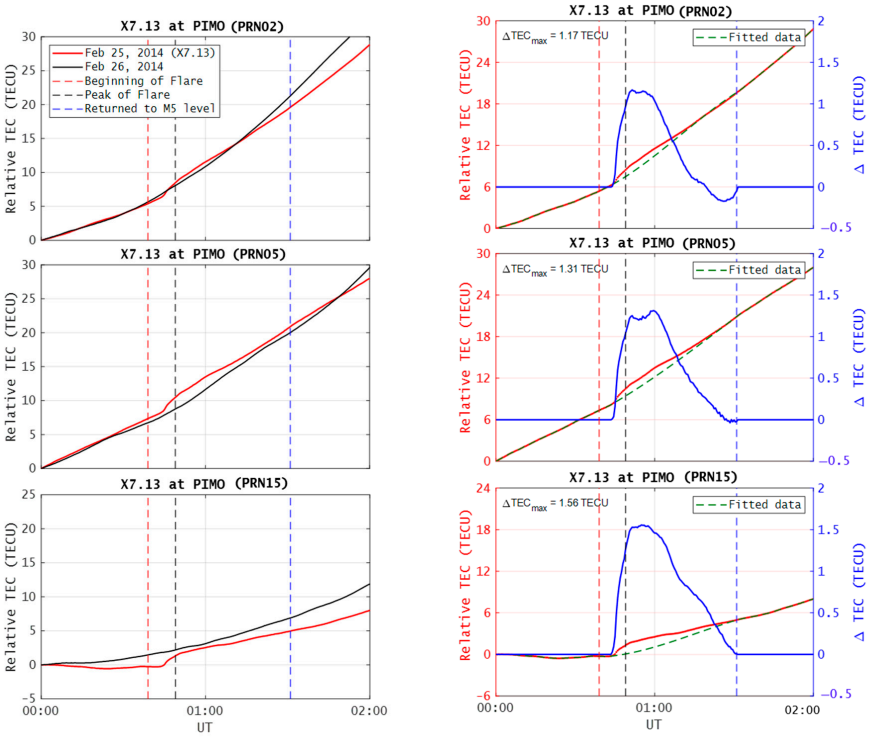

(**a**) (**b**)

Figure 5. (**a**) Superimposed Relative TEC for 25 February (flare day) and 26 February 2014 with the time markers at PIMO; (**b**) (Left axis) Relative TEC for the flare day superimposed with the fitted data and (Right axis) the ΔTEC for the flare day curve. Observation time is from 00:00 UT to 00:02 UT.

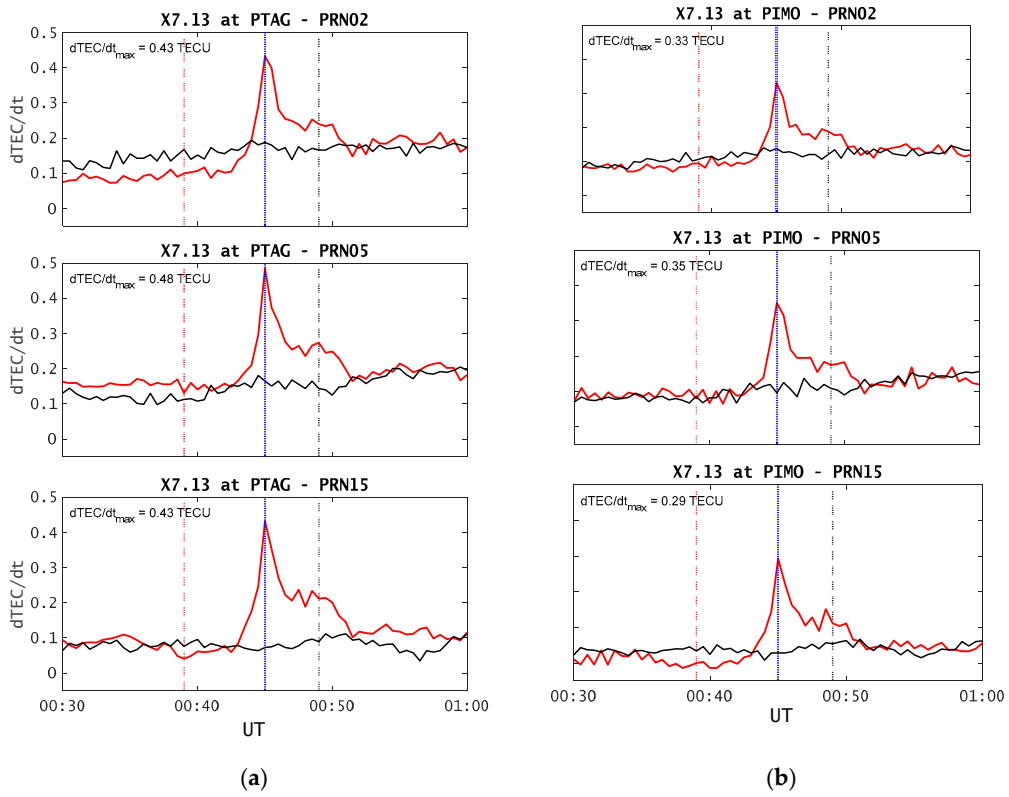

Figure 6. (**a**) Time derivative of TEC per PRN at PTAG (**b**); at PIMO with the observation time 00:30 UT to 01:00 UT. The curves are for the X7.13 day (25 February 2014) and quiet day (26 February 2014). The time markers remain the same: Beginning of flare (red broken vertical line), EUV irradiance peak (blue solid vertical line), and the return to an M5 level (black broken vertical line).

At PTAG, the $dTEC/dt$ maxima reached 0.43, 0.48, and 0.43 TECU/min for PRNs 2, 5, and 15, respectively. At PIMO, these increases are rather lower, reaching 0.33, 0.35, and 0.29 TECU/min. Nonetheless, it can be observed that the increases during the flare day concur with the EUV maximum. This is consistent for both low-latitude stations in the Philippines.

Tsurutani et al. [39] made use of the EUV count (SEM) in investigating four events: 28 October 2003 (X17), 29 October 2003 (X7), 4 November 2003 (X28), and 14 July 2000 (X10). They considered the narrow band channels that provided accurate profiles (e.g., onset, peak count rates, and decays). Using the EUV count, the peak intensity was higher for the X17 than for the X28. The TEC calculations reached ~25 TECU above the background level during the X17, while this was ~5–9 TECU for the remaining flares. The resulting TEC enhancements during the X17 persisted for about 3 h, longer than the flare duration. Photoionization by X-ray was not found to be effective in producing their observed prolonged TEC enhancements. They added as well that recombination rates are low at the middle altitudes within which electron production is increased and photoionization is caused by the EUV.

Mahajan et al. [40] also used the solar X-ray, EUV, and TEC measurements to show the significant correlation between the peak TEC enhancement and peak EUV enhancement. Aside from this, there is also a correlation between the peak TEC enhancement and X-ray flux that improves when considering the central meridian distance (CMD) of the flare site. It was also characterized that the solar EUV range has strong center-to-limb variations [41]. EUV absorption by the solar atmosphere is greater when the flare site is away from the solar disk center. Zhang et al. [42] also suggested that flare eruptions close to the solar meridian produce stronger responses in the ionosphere.

The X7 flare that erupted on 9 August 2011 over the Indian region was also investigated by Sripathi et al. [21]. They have used the Global Positioning System (GPS) for the TEC observations and determined ~2–3 TECU of enhancements. D-region ionization was also considered to have accounted for the increases in the very low frequency (VLF) signal amplitude, which was indicated by the disappearances in the ionogram echoes. During solar flares, radio signals may be absorbed by the ionized D-region. Thomson et al. [43] have also investigated the use of VLF observations when studying electron density in the D-region.

3.3. ΔH and EEJ

Figure 7 shows the geomagnetic responses in the H component for the equatorial and off-equatorial stations as well as the resulting EEJ strength in nT. From Figure 6a, it can be observed that during the X7.13 flare, ΔH is more enhanced at A08 than at MUT. At A08, the curve for the flare day started to rapidly rise shortly before the flare maximum and reached its first peak after the flare maximum, whereas the curve for the quiet day suggests no drastic changes. The EEJ strength is observed to abruptly increase in a similar manner as the ΔH at A08 did. Its corresponding change from the background value was about ~60 nT. Figure 6b shows the ΔH variations individually at CDO and LGZ and also the EEJ. During the flare day, the changes are more pronounced at CDO than at LGZ. At the equatorial CDO, the ΔH starts rising shortly before the flare maximum and eventually reaches its first peak. The corresponding EEJ response is estimated at ~37 nT.

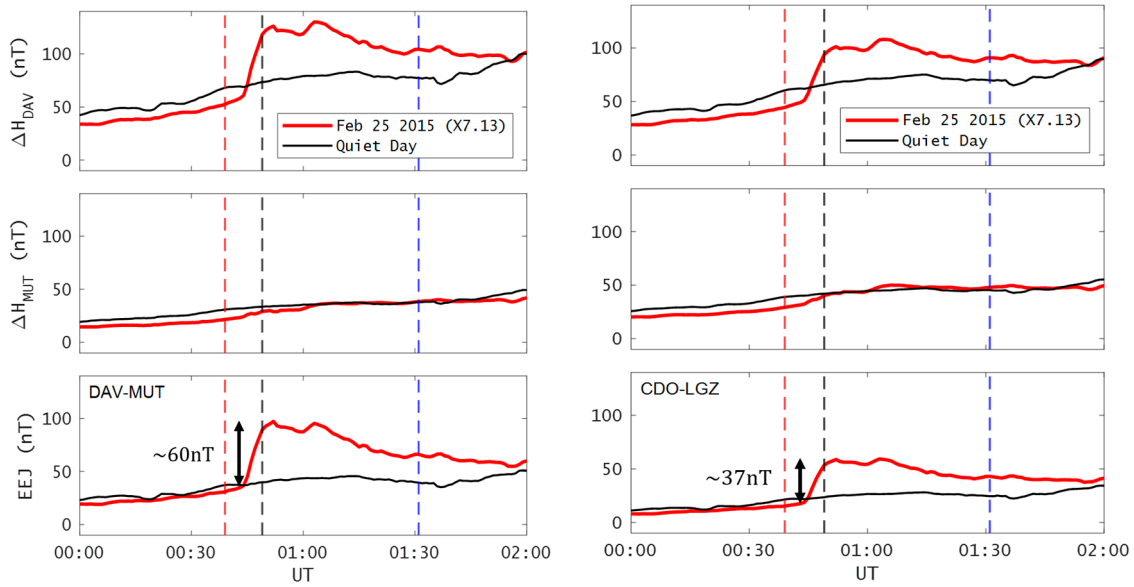

Figure 7. (**a**) ΔH variations in equatorial (A08 or DAV) and off-equatorial (MUT) stations; (**b**) in equatorial (CDO) and off-equatorial (LGZ) stations. Observation time is from 00:00 UT to 00:02 UT.

As soon as the flare reaches its maximum, the EEJ measurements have already been approaching maximum as well. This is consistent with the A08-MUT and CDO-LGZ observations. More so, there is a secondary peak that is observed at around 01:05 UT at the equatorial stations, which is again reflected in the ΔH. This suggests a rather prolonged influence on the geomagnetic field and associated equatorial currents. As for the preflare behavior of the EEJ, there are no observed depressions.

Saharan et al. [38] showed the variability of the ΔH and the EEJ over Indian stations, Tirunelveli (8.7° N, 77.8° E, dip latitude: 0.4° N) and Alibag (18.5° N, 72.9° E, dip latitude: 13.0° N). This was during an X7 flare on 09 August 2011 that peaked at

08:05 UT. The ΔH variations at Tirunelveli (equatorial) reveal slow decreases during the onset of the flare, while at Alibag (low latitude) there were increases. Sudden depression in the EEJ was also observed such that when it reached negative values, it was suggested that a counter electrojet (CEJ) started developing. Unlike in the present study, the equatorial stations show no decreases in the ΔH. Instead, increases in the ΔH were seen as confirmed by the increases in the EEJ. From these observations in different studies, the behaviors in the ΔH are nonetheless always observed to be consistent with the EEJ, especially during the flare maximum.

Rastogi et al. [44] also observed the electrojet strengths over Indo-Russian latitudes. They suggested that during normal electrojet events, the impulses in the H are positive at all stations. It is during strong CEJ periods that ionospheric currents reverse, especially along the equator; hence, the negative impulses in the H observed at equatorial stations. The impulses over low-latitude stations remain positive since they are unaffected by this reversal.

Zhang et al. [45] also presented the ionospheric responses to solar flares while incorporating the related electrodynamics. They studied the flares from 1998 to 2008 and the effects on the EEJ at Jicamarca. Increases in the EEJ were present during the solar flares, such that the EEJ is eastward at preflare stages. This in turn was indicated by the increases in the ΔH.

In contrast to the more intense flare of the present analysis, solar flares of weaker intensities (M, C, and B) are used in the study of Chakrabarty et al. [46]. They investigated the changes in the EEJ current as a response to these flares. It was revealed that these events enhanced the EEJ regardless of the electrojet being a normal one or a counter. They, however, emphasized that investigating the EEJ response corresponding to weaker flares can be appropriately estimated only when the local time variation of the quiet time E-region zonal electric field is considered. It was also found that the E-region electric field modulates EEJ strength.

4. Conclusions and Recommendations

This present work analyzes the effects of an intense X7.13 flare on the ionospheric TEC over the Philippines using low-latitude stations (PIMO and PTAG). In particular, the EUV measurements are given focus to check if the TEC changes concur with the EUV maximum. These were confirmed using the *dTEC/dt* values that maximized at the same time the EUV measurements in W/m^2 did at both stations. The *dTEC/dt* maximum values ranged from 0.29 to 0.48 TECU/min, collectively at both stations. Additionally, the ΔTEC values ranged from 1.17 to 1.97 TECU, collectively at both stations.

The electrojet currents experienced amplifications as a direct product of the increased conductivities due to increased solar radiation during the X7.13 eruption. The ΔH variations and the EEJ strength were investigated. It was inferred that at the equatorial station, the ΔH increases indicate the same behavior on the EEJ strength. Enhancements of the EEJ from the background values are larger for A08 (DAV) than at CDO, with values ~60 nT and ~37 nT, respectively. This is considering that A08 has a dip latitude closer to 0 than CDO does. The dip latitude at the magnetic equator, where conductivities are more enhanced, is 0. This means that A08, whose dip latitude is closer to 0, experiences more enhanced conductivities, thus geomagnetic effects.

In extending this work, the inclusion of other parameters and measurements is recommended. The flare site can be considered to incorporate the center-to-limb variabilities in relation to the EUV emissions. However, this would be more useful when observing additional flares with different solar emission measurements in terms of comparison. Also, GNSS stations near the equatorial magnetometer are ideal to add. This would give more information regarding the TEC measured near those regions.

Author Contributions: Conceptualization, Z.N.C.D. and E.P.M.; methodology, Z.N.C.D. and E.P.M.; software, Z.N.C.D. and E.P.M.; validation, Z.N.C.D. and E.P.M.; formal analysis, Z.N.C.D. and E.P.M.; investigation, Z.N.C.D. and E.P.M.; resources, A.Y.; data curation, Z.N.C.D., E.P.M. and A.Y.; writing—original draft preparation, Z.N.C.D. and E.P.M.; writing—review and editing, Z.N.C.D. and E.P.M.; visualization, Z.N.C.D. and E.P.M.; supervision, E.P.M.; project administration, E.P.M.; funding acquisition, E.P.M. All authors have read and agreed to the published version of the manuscript.

Funding: AMBER is operated by Boston College and funded by NASA and AFOSR.

Data Availability Statement: Data are contained within the article.

Acknowledgments: The authors are thankful to the International Research Center for Space and Planetary Environmental Science (i-SPES), Kyushu University for providing MAGDAS geomagnetic field data. Also, the authors thank the AMBER team for the data. The authors acknowledge the International GNSS Service (IGS) and Crustal Dynamics Data Information System (CDDIS-NASA), Jet Propulsion Laboratory (JPL-NASA), Philippine Active Geodetic Network, National Mapping and Resource Information Authority for providing the GNSS data; the National Oceanic and Atmospheric Administration (NOAA) Geostationary Operational Environmental Satellites (GOES), https://www.ngdc.noaa.gov/stp/satellite/goes-r.html, (accessed on 24 October 2024) and the SOHO Solar EUV Monitor, https://lasp.colorado.edu/eve/data_access/eve_data/ (accessed on 27 October 2024), for the solar data; NASA/Goddard Space Flight Center OMNIWeb, https://omniweb.gsfc.nasa.gov/form/dx1.html (accessed on 1 November 2024), and the GFZ German Research Centre for Geosciences, https://kp.gfz-potsdam.de/en/data (accessed on 1 November 2024), for the geomagnetic data.

Conflicts of Interest: The authors declare no conflicts of interest.

References

1. Liu, L.B.; Wan, W.X.; Chen, Y.D.; Le, H.J. Solar activity effects of the ionosphere: A brief review. *Chin. Sci. Bull.* **2011**, *56*, 1202–1211. [CrossRef]
2. Pavlov, A.V. Ion Chemistry of the Ionosphere at E- and F-Region Altitudes: A Review. *Surv. Geophys.* **2012**, *33*, 1133–1172. [CrossRef]
3. Marov, M.Y.; Kuznetsov, V.D. Solar Flares and Impact on Earth. *Handb. Cosm. Hazards Planet. Def.* **2014**, *1*, 1–26. [CrossRef]
4. Divinagracia, P.P.; Macalalad, E.; Guido, R.M.; Tucio, P.; Kalaw, J. Preliminary Analysis of Satellite Navigation Effects of the Strong Solar Flares during Solar Cycle 24. In Proceedings of the International Conference on Space Science and Communication (IconSpace), Selangor, Malaysia, 23–24 November 2021; pp. 109–112. [CrossRef]
5. Benz, A.O. Flare Observations. *Living Rev. Sol. Phys.* **2017**, *14*, 2. [CrossRef]
6. Richmond, A.D. The Ionosphere and Upper Atmosphere. *Sun Auroras Magn. Storms Sol. Flares Cosm. Rays* **2011**, *50*, 35–44. [CrossRef]
7. Lysak, R.L. Electrodynamic Coupling of the Magnetosphere and Ionosphere. *Space Sci. Rev.* **1990**, *52*, 33–87. [CrossRef]
8. Maglambayan, V.L.L.; Macalalad, E.P. Two-Dimensional Mapping of Ionospheric Total Electron Content over the Philippines Using Kriging Interpolation. *Atmosphere* **2022**, *13*, 1626. [CrossRef]
9. Mendoza, M.M.; Macalalad, E.P.; Juadines, K.E.S. Analysis of the Ionospheric Total Electron Content during the Series of September 2017 Solar Flares over the Philippine—Taiwan Region. In Proceedings of the 2019 6th International Conference on Space Science and Communication (IconSpace), Johor Bahru, Malaysia, 28–30 July 2019; pp. 182–185. [CrossRef]
10. Nagata, T. Characteristics of the Solar Flare Effect (*Sqa*) on Geomagnetic Field at Huancayo (Peru) and at Kakioka (Japan). *J. Geophys. Res.* **1952**, *57*, 1–14. [CrossRef]
11. Yamazaki, Y.; Maute, A. Sq and EEJ—A Review on the Daily Variation of the Geomagnetic Field Caused by Ionospheric Dy-namo Currents. *Space Sci. Rev.* **2017**, *206*, 299–405. [CrossRef]
12. Richmond, A.D. Ionospheric Wind Dynamo Theory: A Review. *J. Geomagn. Geoelectr.* **1979**, *31*, 287–310. [CrossRef]
13. Wagner, C.U.; Möhlmann, D.; Schäfer, K.; Mishin, V.M.; Matveev, M.I. Large-scale electric fields and currents and related geomagnetic variations in the quiet plasmasphere. *Space Sci. Rev.* **1980**, *26*, 391–446. [CrossRef]
14. Bolaji, O.S.; Oyeyemi, E.O.; Owolabi, O.P.; Yamazaki, Y.; Rabiu, A.B.; Okoh, D.; Fujimoto, A.; Amory-Mazaudier, C.; Seemala, G.K.; Yoshikawa, A.; et al. Solar Quiet Current Response in the African Sector due to a 2009 Sudden Stratospheric Warming Event. *J. Geophys. Res. Space Phys.* **2016**, *121*, 8055–8065. [CrossRef]
15. Zhang, P.; Sun, Y.Y.; Chen, C.H.; Mao, Z. Two-Step Method for Determining the Solar Quiet Current Focus and the Validation Using Observing Procedure Experiment. *Earth Space Sci.* **2023**, *10*, e2022EA002572. [CrossRef]

16. Lühr, H.; Alken, P.; Zhou, Y.L. The Equatorial Electrojet. In *Ionosphere Dynamics and Applications*; Wiley: Hoboken, NJ, USA, 2021; pp. 281–299. ISBN 9781119815617.
17. Bhattacharyya, A. Equatorial Electrojet. In *Encyclopedia of Solid Earth Geophysics*; Springer: Cham, Switzerland, 2020; pp. 1–3. [CrossRef]
18. Ismail, W.N.I.; Hamid, N.S.A.; Abdullah, M.; Yoshikawa, A.; Uozumi, T.; Radzi, Z.M. Comparison of EEJ Longitudinal Variation from Satellite and Ground Measurements over Different Solar Activity Levels. *Universe* **2021**, *7*, 23. [CrossRef]
19. Chapman, S. *The Equatorial Electrojet as Detected from the Abnormal Electric Current Distribution Above Huaneayo, Peru, and Elsewhere*; SCIRP: Wuhan, China, 1951.
20. Gopika, P.G.; Ambili, K.M.; Choudhary, R.K. The Response of the D and E Regions of the Equatorial Ionosphere to Solar Flare Events. *J. Geophys. Res. Space Phys.* **2021**, *126*, e2021JA029350. [CrossRef]
21. Sripathi, S.; Balachandran, N.; Veenadhari, B.; Singh, R.; Emperumal, K. Response of the Equatorial and Low-Latitude Ionosphere to an Intense X-Class Solar Flare (X7/2B) as observed on 9 August 2011. *J. Geophys. Res. Space Phys.* **2013**, *118*, 2648–2659. [CrossRef]
22. Machol, J.; Codrescu, S.; Peck, C. User's Guide for GOES-R XRS L2 Products. Available online: https://www.ngdc.noaa.gov/stp/satellite/goes-r.html (accessed on 13 December 2024).
23. Kataoka, R. *Extreme Space Weather. Extreme Space Weather*; Elsevier: Amsterdam, The Netherlands, 2022; pp. 1–176. [CrossRef]
24. MacAlester, M.H. Extreme Space Weather and Emergency Management. *Extrem. Events Geosp. Orig. Predict. Conseq.* **2018**, *1*, 683–700. [CrossRef]
25. Yamazaki, Y.; Matzka, J.; Stolle, C.; Kervalishvili, G.; Rauberg, J.; Bronkalla, O.; Morschhauser, A.; Bruinsma, S.; Shprits, Y.Y.; Jackson, D.R. Geomagnetic Activity Index Hpo. *Geophys. Res. Lett.* **2022**, *49*, e2022GL098860. [CrossRef]
26. Matzka, J.; Stolle, C.; Yamazaki, Y.; Bronkalla, O.; Morschhauser, A. The Geomagnetic *Kp* Index and Derived Indices of Geomagnetic Activity. *Space Weather* **2021**, *19*, e2020SW002641. [CrossRef]
27. Noll, C.E. The Crustal Dynamics Data Information System: A Resource to Support Scientific Analysis Using Space Geodesy. *Adv. Space Res.* **2010**, *45*, 1421–1440. [CrossRef]
28. Singh, A.K.; Tiwari, S. *Atmospheric Remote Sensing: Principles and Applications*; Elsevier: Amsterdam, The Netherlands, 2022; pp. 1–462. [CrossRef]
29. Wang, X.-L.; Wan, Q.-T.; Ma, G.-Y.; Li, J.-H.; Fan, J.-T. The Influence of Ionospheric Thin Shell Height on TEC Retrieval from GPS Observation. *Res. Astron. Astrophys.* **2016**, *16*, 116. [CrossRef]
30. Chen, H.; Miao, M.; Chang, Y.; Wang, Q.; Shen, X.; Hattori, K.; Han, P. Singular Spectrum Analysis of the Total Electron Content Changes Prior to M $\geq$ 6.0 Earthquakes in the Chinese Mainland During 1998–2013. *Front. Earth Sci.* **2021**, *9*, 677163. [CrossRef]
31. Ansari, K.; Sharma, S.K. Ionospheric TEC Variation Based on GNSS Data Over the Arabian Peninsula and Validation with the Cubic Spline Interpolated GIM Model. *Adv. Space Res.* **2021**, *68*, 3814–3820. [CrossRef]
32. Maletckii, B.; Yasyukevich, Y.; Vesnin, A. Wave Signatures in Total Electron Content Variations: Filtering Problems. *Remote Sens.* **2020**, *12*, 1340. [CrossRef]
33. Yizengaw, E.; Moldwin, M.B. African Meridian B-Field Education and Research (AMBER) Array. *Earth Moon Planets* **2009**, *104*, 237–246. [CrossRef]
34. Yumoto, K.; Group, C. Characteristics of Pi 2 Magnetic Pulsations Observed at the CPMN Stations: A Review of the STEP Results. *Earth Planets Space* **2001**, *53*, 981–992. [CrossRef]
35. Rastogi, R.G.; Klobuchar, J.A. Ionospheric Electron Content Within the Equatorial F_2 Layer Anomaly Belt. *J. Geophys. Res.* **1990**, *95*, 19045–19052. [CrossRef]
36. Sergeeva, M.A.; Maltseva, O.A.; Vesnin, A.M.; Blagoveshchensky, D.V.; Gatica-Acevedo, V.J.; Gonzalez-Esparza, J.A.; Chernov, A.G.; Orrala-Legorreta, I.D.; Melgarejo-Morales, A.; Gonzalez, L.X.; et al. Solar Flare Effects Observed over Mexico during 30–31 March 2022. *Remote Sens.* **2023**, *15*, 397. [CrossRef]
37. Pandey, K.; Chakrabarty, D.; Kumar, A.; Bhardwaj, A.; Biswal, S.; Hussey, G.; Yadav, A. Characteristics of X-Class Flares of Solar Cycles 23 and 24 in X-Ray and EUV Bands. *Adv. Space Res.* **2023**, *71*, 5438–5452. [CrossRef]
38. Saharan, S.; Maurya, A.K.; Dube, A.; Patil, O.M.; Singh, R.; Sharma, H. Low latitude ionospheric TEC response to the solar flares during the peak of solar cycle 24. *Adv. Space Res.* **2023**, *72*, 3890–3902. [CrossRef]
39. Tsurutani, B.T.; Judge, D.L.; Guarnieri, F.L.; Gangopadhyay, P.; Jones, A.R.; Nuttall, J.; Zambon, G.A.; Didkovsky, L.; Mannucci, A.J.; Iijima, B.; et al. The 28 October 2003 Extreme EUV Solar Flare and Resultant Extreme Ionospheric Effects: Comparison to Other Halloween Events and the Bastille Day Event. *Geophys. Res. Lett.* **2005**, *32*, 1–4. [CrossRef]
40. Mahajan, K.K.; Lodhi, N.K.; Upadhayaya, A.K. Observations of X-Ray and EUV Fluxes During X-Class Solar Flares and Response of Upper Ionosphere. *J. Geophys. Res.* **2010**, *115*, 12330. [CrossRef]
41. Donnelly, R.F. Empirical Models of Solar Flare X Ray and EUV Emission for Use in Studying Their and Region Effects. *J. Geophys. Res.* **1976**, *81*, 4745–4753. [CrossRef]

42. Zhang, D.; Xiao, Z.; Chang, Q. The Correlation of Flare's Location on Solar Disc and the Sudden Increase of Total Electron Content. *Chin. Sci. Bull.* **2002**, *47*, 82–85. [CrossRef]
43. Thomson, N.R.; Clilverd, M.A. Solar Flare Induced Ionospheric D-Region Enhancements from VLF Amplitude Observations. *J. Atmos. Sol.-Terr. Phys.* **2001**, *63*, 1729–1737. [CrossRef]
44. Rastogi, R.G.; Pathan, B.M.; Rao, D.R.K.; Sastry, T.S.; Sastri, J.H. Solar Flare Effects on the Geomagnetic Elements During Normal and Counter Electrojet Periods. *Earth Planets Space* **1999**, *51*, 947–957. [CrossRef]
45. Zhang, R.; Liu, L.; Le, H.; Chen, Y. Equatorial Ionospheric Electrodynamics During Solar Flares. *Geophys. Res. Lett.* **2017**, *44*, 4558–4565. [CrossRef]
46. Chakrabarty, D.; Bagiya, M.S.; Thampi, S.V.; Pathan, B.M.; Sekar, R. Signatures of Moderate (M-Class) and Low (C and B Class) Intensity Solar Flares on the Equatorial Electrojet Current: Case studies. *J. Atmos. Sol.-Terr. Phys.* **2013**, *105–106*, 170–180. [CrossRef]